

Improved Auger recombination models: Consequences for c-Si solar cells

Lachlan E. Black ^{*}, Daniel H. Macdonald

School of Engineering, Building 31, The Australian National University, Canberra ACT 2600, Australia



ARTICLE INFO

Keywords:

Crystalline silicon
Auger recombination
Solar cells
Doping

ABSTRACT

Recently, the parameterisation of Auger recombination in c-Si has been revised by two separate studies, both of which reached very similar conclusions. A key change is that the ratio of the Auger coefficients for *n*- and *p*-type Si (C_n/C_p) has been found to be significantly lower than previously accepted. In this work, we explore the implications of these findings for c-Si solar cells. In particular, we seek to answer the question of whether any intrinsic advantage is expected for *n*-type vs *p*-type doping for c-Si solar cells in general, or for particular device architectures. We focus on simple analytical parameters and models in order to elucidate the relevant physical mechanisms, making use of more complex numerical modelling to complement these and validate our conclusions. A key conclusion is that the new models predict improved intrinsic performance potential for *n*-type devices, with *p*-type Si retaining an intrinsic advantage only when surface recombination and transport losses are very close to zero. *n*-type quickly becomes more efficient when non-zero surface recombination is introduced, and widens its advantage with increasing surface saturation current density J_0 . In particular, *n*-type back-junction devices show higher efficiency potential and less sensitivity to bulk resistivity variation than *p*-type equivalents, thanks to lower lateral transport losses for majority carriers in the Si bulk. Meanwhile, an analysis of the intrinsic performance potential of highly doped *n*- and *p*-type Si reveals no significant intrinsic advantage for either type as transport layers.

1. Introduction

Auger recombination is the dominant intrinsic carrier recombination process in crystalline Si (c-Si), and plays an important role in determining the theoretically achievable efficiency limit for c-Si solar cells. Since 2012, the accepted model for Auger recombination in c-Si has been that of Richter et al. [1]. However, for a number of years it has been apparent that the former work significantly overestimates the extent of Auger recombination, particularly in *n*-type material.

Very recently, Black & Macdonald [2] have presented a novel method for determining the Auger coefficients. They have applied this technique to establish a revised parameterisation of Auger recombination in c-Si which is consistent with the available experimental data. Separately, another revision of the Auger model has been performed by Niewelt et al. [3] on the basis of measurements of a state-of-the-art sample set. The resulting parameterisations of Black & Macdonald and Niewelt et al. are in very good agreement, and confirm that Auger recombination in light and moderately doped c-Si is lower than previously thought, especially for *n*-type material.

A key change in the revised parameterisations compared to that of

Richter et al. is a significant reduction in the ratio of the Auger coefficients for *n*- and *p*-type material (C_n/C_p) from 4.84 in Richter et al. to 2.81 (Black and Macdonald) or 2.62 (Niewelt et al.), as shown in Fig. 1a. Interestingly, these revised values are quite close to the ratio of the electron and hole mobilities in lightly doped Si, $\mu_e/\mu_h \approx 3$ [4] (Fig. 1b). Since the low-injection Auger lifetime is given by $(C_p p_0^2)^{-1}$ for *p*-type and $(C_n n_0^2)^{-1}$ for *n*-type Si, an *n*-type wafer, which has an equilibrium majority carrier concentration n_0 that is ~ 3 times (μ_e/μ_h) smaller than the equilibrium majority carrier concentration p_0 in a *p*-type wafer of the same resistivity, will have an Auger lifetime (in low injection) that is roughly $(\mu_e/\mu_h)^2 \times C_p/C_n \approx 3^2 \times 1/3 \approx 3$ times longer. On the other hand, in the *n*-type wafer, the minority carriers are holes, which have a 3 times lower mobility, so that the minority carrier diffusion length (proportional to the square root of the product of lifetime and mobility) will be similar for both *n*- and *p*-type samples.

In operation, solar cells must balance transport and recombination losses to maximise efficiency. It is therefore interesting to consider whether, based on these updated models, there is in any intrinsic advantage to the use of *n*-type vs *p*-type doping in c-Si solar cells in general, or for particular cell architectures. In this contribution, we

* Corresponding author.

E-mail address: lachlan.black@anu.edu.au (L.E. Black).

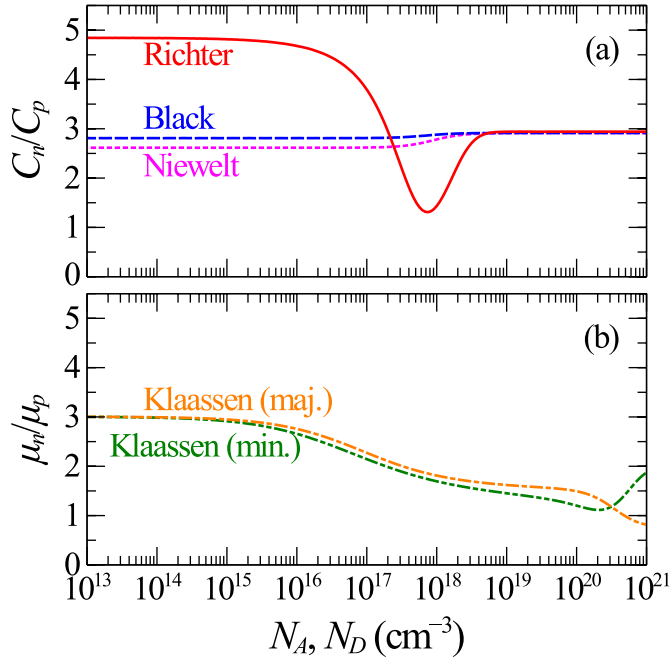


Fig. 1. Ratio of a) Auger coefficients (C_n/C_p) and b) mobilities (μ_n/μ_p) for electrons and holes, as a function of dopant concentration in n - and p -type Si respectively under low injection, according to the Auger parameterisations of Richter et al. [1], Black & Macdonald [2], and Nieuwelt et al. [3], and the mobility model of Klaassen et al. [4]. Mobility ratios are shown for electrons and holes both as majority carriers (i.e. in n - and p -type Si) and as minority carriers (i.e. in p - and n -type Si).

examine this question, focusing on simple analytical parameters and models in order to elucidate the physical mechanisms. More complex numerical device modelling is used to complement and validate the analytical models.

2. Results and discussion

2.1. Analytical models

We begin by considering the minority carrier diffusion length $L_{min} = \sqrt{\tau_{eff} D_{min}}$ (where τ_{eff} is the effective carrier lifetime and D_{min} is the minority carrier diffusion coefficient), a parameter which combines the influence of recombination and transport losses, and which is important for current collection in solar cells. Fig. 2a shows L_{min} (divided by resistivity ρ in order to allow relative variations to be more easily distinguished) as a function of bulk resistivity in n - and p -type Si, for various parameterisations of the intrinsic bulk lifetime, and the mobility model of Klaassen et al. [4]. Note that in these calculations and those that follow we assume complete photon recycling [5], so that radiative recombination is effectively zero and the intrinsic lifetime is equal to the Auger lifetime in all cases. Fig. 2b shows the corresponding ratio between L_{min} for n - and p -type Si as a function of resistivity. The parameterisation of Richter et al. predicts a longer minority carrier diffusion length in p -type than in n -type c-Si of the same resistivity in the resistivity range commonly used for the bulk of c-Si solar cells ($0.1\text{--}10 \Omega \text{ cm}$). By contrast, the new parameterisations of Black & Macdonald and Nieuwelt predict somewhat longer minority carrier diffusion lengths for n -type material in this range.

In practice of course, the intrinsic diffusion length will be much longer than typical device dimensions (e.g. values at $1 \Omega \text{ cm}$ are on the order of tens of mm). Differences in intrinsic bulk lifetime therefore serve mainly to influence the device voltage rather than the current. This effect can be quantified by looking at the implied open-circuit voltage vs

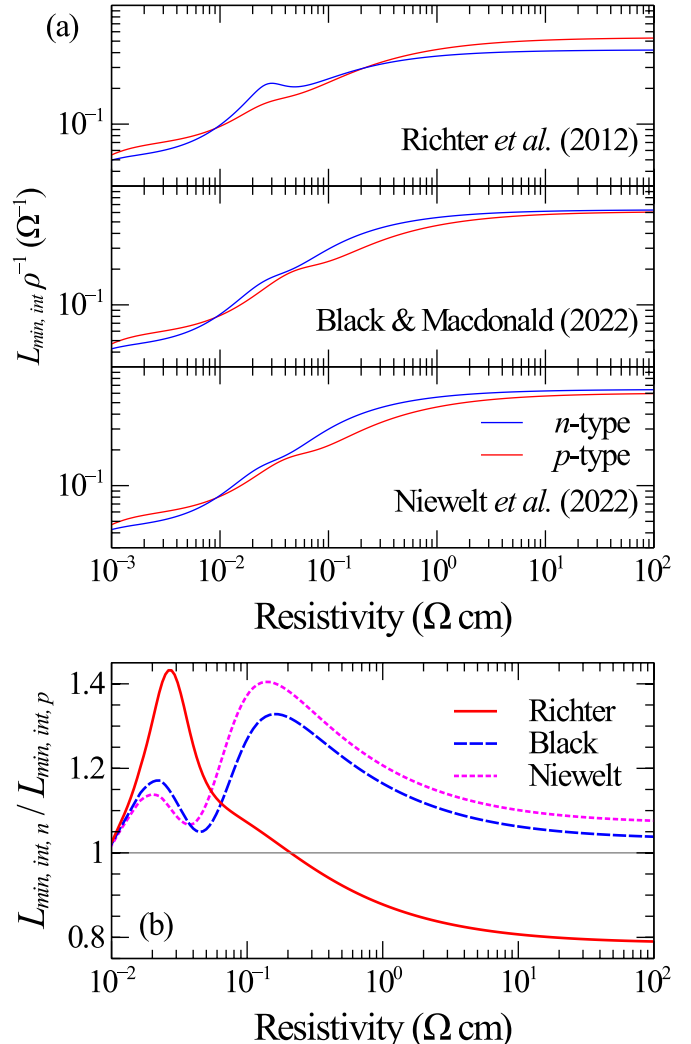


Fig. 2. a) Intrinsic minority-carrier diffusion length $L_{min, int}$ divided by equilibrium resistivity ρ , as a function of equilibrium resistivity for n - and p -type c-Si at 300 K, for different parameterisations of the Auger carrier lifetime, and the mobility model of Klaassen. b) Corresponding ratio of minority carrier diffusion lengths in n - and p -type Si as a function of resistivity.

current density (iV_{oc} vs iJ), which can be calculated directly from the injection-dependent lifetime τ_{eff} (Δn), given values for the device thickness W and generation current density J_{gen} , according to [6].

$$iV_{oc} = \frac{kT}{q} \ln \left[\frac{\Delta n(N + \Delta n)}{n_{i,eff}} \right] \quad (1)$$

$$iJ = J_{gen} - \frac{q W \Delta n}{\tau_{eff}(\Delta n)} \quad (2)$$

where k is the Boltzmann constant, T is temperature, q is the electron charge, Δn is the excess carrier concentration, N is the dopant concentration, and $n_{i,eff}$ is the effective intrinsic carrier concentration (including bandgap narrowing). By varying Δn , one can then generate an implied curve of current density vs voltage. This is essentially equivalent to the implied J-V curve resulting from a conventional Suns- V_{oc} measurement [7]. From such curves, one can calculate an implied power density, and thus a pseudo efficiency, which represents the limiting conversion efficiency that could be obtained in the absence of transport losses.

Fig. 3 plots the pseudo efficiency obtained in this way as a function of equilibrium resistivity for n - and p -type Si, assuming a device thickness

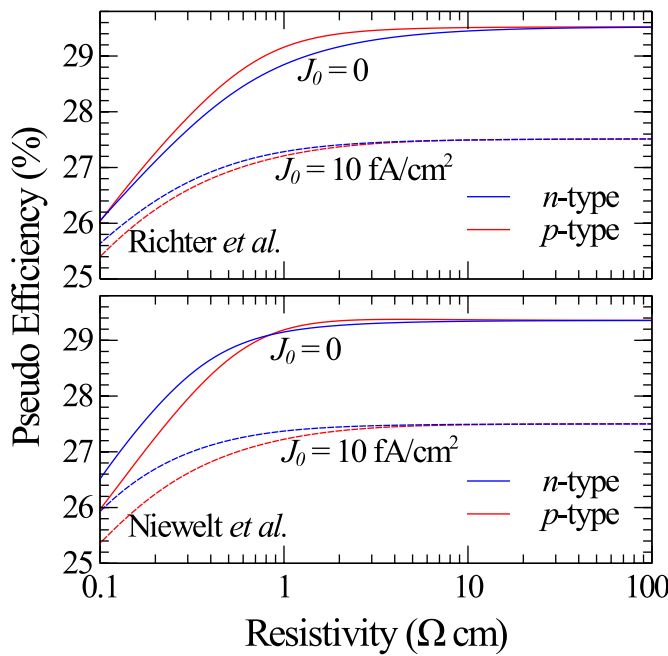


Fig. 3. Pseudo efficiency (100 μm thickness, $J_{sc} = 43.4 \text{ mA}/\text{cm}^2$) vs resistivity for n - and p -type Si, calculated either with the Auger parameterisation of Richter et al., or of Nieuwelt et al. Cases with zero surface recombination and with total $J_0 = 10 \text{ fA}/\text{cm}^2$ are shown.

of 100 μm and $J_{gen} = 43.4 \text{ mA}/\text{cm}^2$ (this thickness and current correspond to the intrinsic efficiency limit for Si cells obtained by Nieuwelt et al. [3]). The effective lifetime τ_{eff} is calculated according to

$$\tau_{eff}^{-1} = \tau_{int}^{-1} + J_0 \frac{\Delta n(N + \Delta n)}{Wqn_{i,eff}^2} \quad (3)$$

assuming $n_{i,eff} = 8.6 \times 10^9 \text{ cm}^{-3}$ where $n_{i,eff}$ is calculated using the model of Misiakos and Tsamakis [8] together with the bandgap narrowing model of Schenk et al. [9], and the intrinsic lifetime τ_{int} is given by the parameterisation of either Richter et al. or Nieuwelt et al. (here and subsequently we choose not to also show calculations using the model of

Black and Macdonald since the model is so similar to that of Nieuwelt et al.). In all cases we assume zero radiative recombination (complete photon recycling). Notably this results in a pseudo efficiency value of 29.4% for intrinsic doping and the lifetime of Nieuwelt et al., in agreement with the value obtained by the latter via more complex numerical simulations.

Fig. 3 shows that the Auger parameterisation of Richter et al. predicts a consistently higher pseudo efficiency potential for p -type than for n -type Si of the same resistivity when surface recombination is not present. In contrast, the parameterisation of Nieuwelt et al. predicts only a narrow advantage for p -type Si in the range between ~ 1 and $10 \Omega\text{ cm}$, with a significant advantage for n -type at lower resistivities. In both cases the advantage shifts towards n -type when a surface recombination component with $J_0 = 10 \text{ fA}/\text{cm}^2$ is added.

As noted above, this analysis excludes the impact of possible transport losses. The extent of such transport losses obviously depends on the integrated product of the local resistivities and currents for each carrier type. Here it should be noted that significant excess carriers are present at the maximum power point (MPP) and will contribute to the bulk conductivity for both majority and minority carriers. Therefore, one should consider the total conductivity (or equivalently, resistivity) due to the total concentration of majority or minority carriers under MPP conditions.

In Fig. 4a we plot the effective majority and minority carrier resistivities at maximum power point (MPP) corresponding to the cases represented in Fig. 3. One can distinguish two limiting regimes in these figures: i) at higher resistivities the ratio between the non-equilibrium majority-(minority-) carrier resistivities in p - and n -type Si simply approaches the ratio of the electron (hole) and hole (electron) mobilities, because the bulk is approaching high injection ($\Delta n \gg N$) and the concentrations of electrons and holes are therefore roughly equal ($n \approx p$); ii) at low resistivities we have the opposite situation ($\Delta n \ll N$), so the majority carrier resistivity approaches the equilibrium value, and the ratio between the minority carrier resistivities now depends also on the minority carrier concentration and thus on the lifetime at each resistivity.

In case i, the corresponding pseudo efficiency values (Fig. 3) are similar for n - and p -type Si, so that transport losses can be expected to make the difference in actual device efficiency. Here the higher mobility of electrons clearly results in a lower resistivity for majority carriers and a higher resistivity for minority carriers in n -type Si than in p -type. Of

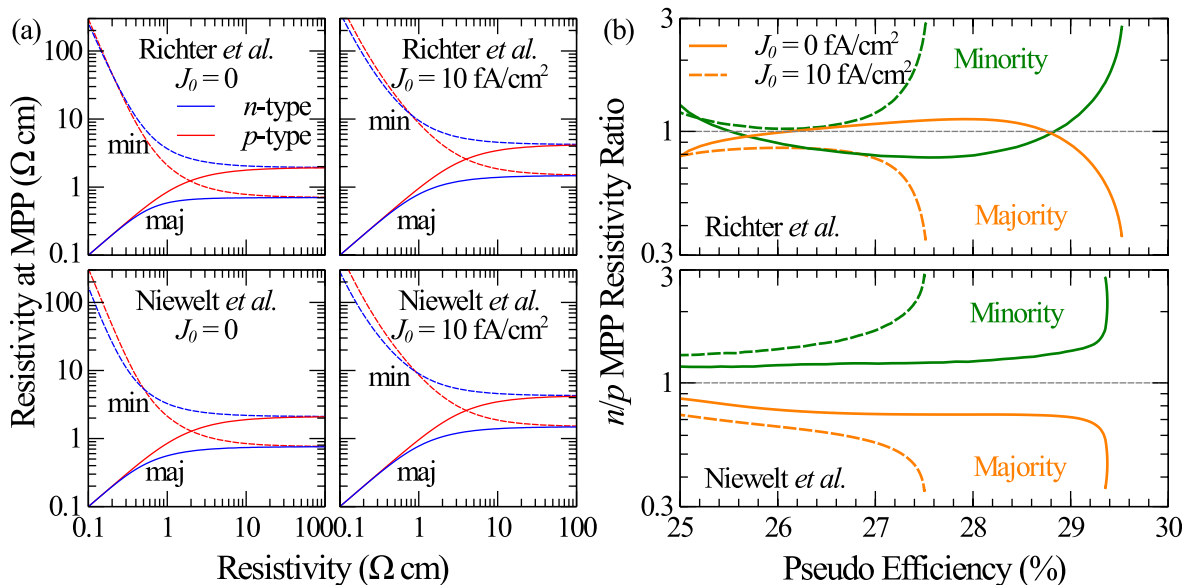


Fig. 4. a) Effective non-equilibrium resistivity for both majority and minority carriers at the pseudo maximum power point (MPP), corresponding to the cases shown in Fig. 3, as a function of equilibrium resistivity. Solid lines show effective resistivities for majority carriers, while dashed lines show effective resistivities for minority carriers. b) Corresponding ratio of MPP resistivity in n -type to that in p -type Si for both majority and minority carriers as a function of the pseudo efficiency.

course, at the highest resistivities, where high-injection conditions obtain in their strictest sense, the difference in doping type becomes academic, since the carrier concentration is independent of doping at MPP (hence the efficiency also becomes identical for *n*- and *p*-type in this limit). In case ii, the majority carrier resistivities are similar, but the pseudo efficiency is significantly higher for *n*-type than for *p*-type Si at a given equilibrium resistivity according to the new Auger parameterisations (Fig. 3). Consequently, for a given pseudo efficiency, the majority carrier resistivity at MPP will actually still be lower for *n*-type Si than for *p*-type in this range as well.

This can be seen more clearly in Fig. 4b, which plots the corresponding ratios between the majority and minority carrier resistivities in *n*-type to those in *p*-type Si at the same pseudo efficiency. The point here is to examine which doping type has an advantage in terms of transport losses when recombination losses are the same. For the Auger parameterisation of Richter et al., the effective majority carrier resistivity for *n*- and *p*-type Si at a given pseudo efficiency is quite similar over much of the range below the highest pseudo efficiency levels (from comparison to Fig. 3, this corresponds to the low-resistivity range). However, using the new parameterisations of Niewelt et al. and Black & Macdonald (the latter not shown), the effective majority carrier resistivity remains significantly lower for *n*-type than for *p*-type Si of the same pseudo efficiency potential over the whole range. Therefore, there may be an intrinsic advantage to using *n*-type material in devices where majority carrier transport is an important loss mechanism, e.g. in back-junction devices without a front transport layer. On the other hand, the effective minority carrier resistivity for *n*-type Si is consistently higher than for *p*-type Si of the same pseudo efficiency potential. Therefore, *p*-type material may be advantageous in device architectures where minority carrier transport is important, such as front-junction devices.

2.2. Numerical simulations

In order to validate these hypotheses, we have also performed full numerical simulations using Quokka3 [10]. For these simulations we assumed ideal (Lambertian) light-trapping, as used previously to determine intrinsic efficiency limits for Si cells. We treat contacts as optically transparent (zero contact shading) with zero contact resistance and zero transport losses in the metal. Only intrinsic bulk recombination is considered, using the Auger models of either Richter et al. or Niewelt et al., together with the radiative model of Nguyen et al. [11] (photon recycling is calculated based on the same optical model used for generation in both cases). Surface recombination is included in the form of a uniform J_0 term divided equally between front and rear, and calculated assuming $n_{i,\text{eff}} = 8.6 \times 10^9 \text{ cm}^{-3}$. Bulk transport losses are included as normal. We consider both *n*- and *p*-type front-junction (FJ) and back-junction (BJ) devices (the latter are obtained by simply switching the polarity of the front and back contacts in the simulation; both architectures have contacts on both sides).

We start by considering a nearly ideal 1D structure with full-area front and rear contacts, in which lateral transport losses are therefore not present (this could equivalently be thought of as a structure with ideal, lossless transport layers). Besides possible carrier profile non-uniformities and vertical transport losses, this structure thus closely resembles the case modelled in Fig. 3. The resulting simulated efficiencies are shown in Fig. 5 as a function of bulk resistivity and for varying total J_0 . Using the Richter Auger parameterisation, *p*-type Si has a clear advantage in the ideal case without surface recombination ($J_0 = 0$). However this advantage narrows significantly under the new Auger models. When a non-zero J_0 is introduced, *n*-type Si gains a slight advantage, which increases with increasing J_0 , and is further emphasised under the new Auger models. These results are closely consistent with those obtained by the simpler analytical approach (Fig. 3), as expected. Note that in this scenario back-junction devices perform slightly

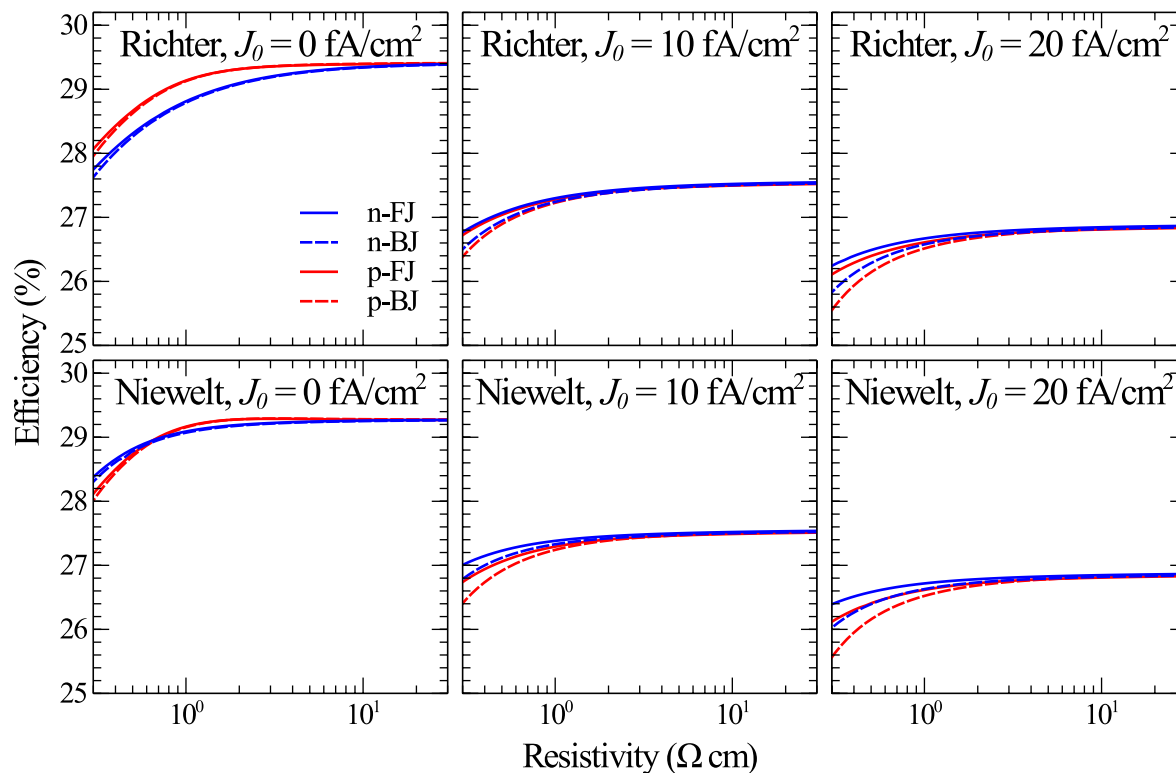


Fig. 5. Simulated (Quokka3) conversion efficiency as a function of wafer resistivity for *n*- and *p*-type front-junction (FJ) and back-junction (BJ) devices with full-area transparent front and back contacts and a wafer thickness of 100 μm. Cases are shown using the Auger parameterisations of Richter et al. and of Niewelt et al., and for varying total J_0 .

worse than front-junction, particularly at lower resistivities, since minority carrier resistivities in this range are sufficiently high to cause significant vertical transport losses for such structures (Fig. 4a), while lateral transport losses are not present.

In the idealised structures considered in Fig. 5, the peak efficiencies actually occur at the highest resistivities, i.e. in close-to-intrinsic material. In actual devices, this picture is complicated both by the existence of extrinsic bulk recombination, to which high-resistivity devices are more sensitive, as well as lateral bulk transport losses. We therefore next consider a device configuration in which the full-area front contact is replaced with front line-contacts (40 μm width), without a front transport layer. We continue to assume no shading or resistance losses from these line contacts (zero contact and line resistance). We omit a transport layer partly because its inclusion would complicate the focus only on intrinsic losses, but also because the omission of a conventional diffused transport layer practically allows for very low front J_0 , which is required to achieve high efficiencies. This architecture has also recently demonstrated very high efficiencies (26.0%) experimentally in *p*-type back-junction devices [12]. Of course, an alternative to diffused transport layers is the use of an external transport layer, such as the transparent conductive oxide layer in silicon heterojunction devices, or the doped poly-Si layer in a tunnel-oxide/poly-Si stack. This also allows a low J_0 to be retained, but presents a different trade-off with parasitic absorption losses that limit device current and thus efficiency.

Fig. 6 shows the resulting simulated efficiencies as a function of bulk resistivity with a front-contact pitch of 1 mm, again for varying total J_0 . Under the Richter parameterisation, the *p*-type devices still have an advantage when the surface recombination is zero. However, under the revised Auger models, the *n*-type back-junction device already matches the performance of the *p*-type devices, both front- and back-junction, and with increasing J_0 it significantly outperforms them. Furthermore, its efficiency is also significantly less sensitive to resistivity variation, with an almost constant efficiency for resistivities of $\sim 1 \Omega\text{ cm}$ or above.

In contrast, the efficiency of the *p*-type back-junction device noticeably suffers at higher resistivities because the majority carriers which must provide lateral conduction are holes, which have a lower mobility than electrons. This is exacerbated with increasing J_0 because the excess carrier concentration available for lateral conduction at MPP is reduced.

Notice also that in this case the efficiency of both front-junction devices is significantly lower than the back-junction devices at low resistivities, which is the reverse of the case in Fig. 5. This is because the major transport loss is now due to lateral transport of carriers to the front contacts, which for the front-junction devices are minority carriers, which are in short supply at low resistivities (c.f. Fig. 4a). The *n*-type front-junction device performs worst here because it has the highest effective resistivity for lateral transport of the relevant carriers (holes in this case). A consequence of this is that the *p*-type front-junction device would require a less conductive transport layer to support lateral conduction of minority carriers than would the *n*-type front-junction device (at least outside of the low resistivity range), which could either allow a lower front J_0 or reduced optical losses in an external transport layer.

As might be expected, the advantage of the *n*-type back-junction device increases with increasing finger pitch, as shown in Fig. 7, where we show results for pitches between 0.5 and 1.5 mm, with a fixed J_0 of 10 fA/cm². Again, this is due to greater lateral transport losses for the *p*-type back-junction device due to the lower mobility of holes. Meanwhile, the *p*-type front-junction device only approaches the efficiency of the *n*-type back-junction device at high resistivities.

Up to this point we have been considering devices with an absorber thickness of 100 μm . This is because this is close to the optimum for ideal devices with no surface recombination [3]. Of course, with increasing surface recombination, the optimum thickness will increase. Increasing thickness also helps to mitigate lateral transport losses by providing a larger bulk cross-section for lateral conduction. Therefore, an obvious question would be whether the *n*-type back-junction device retains its advantage when we consider increased wafer thickness. To help answer

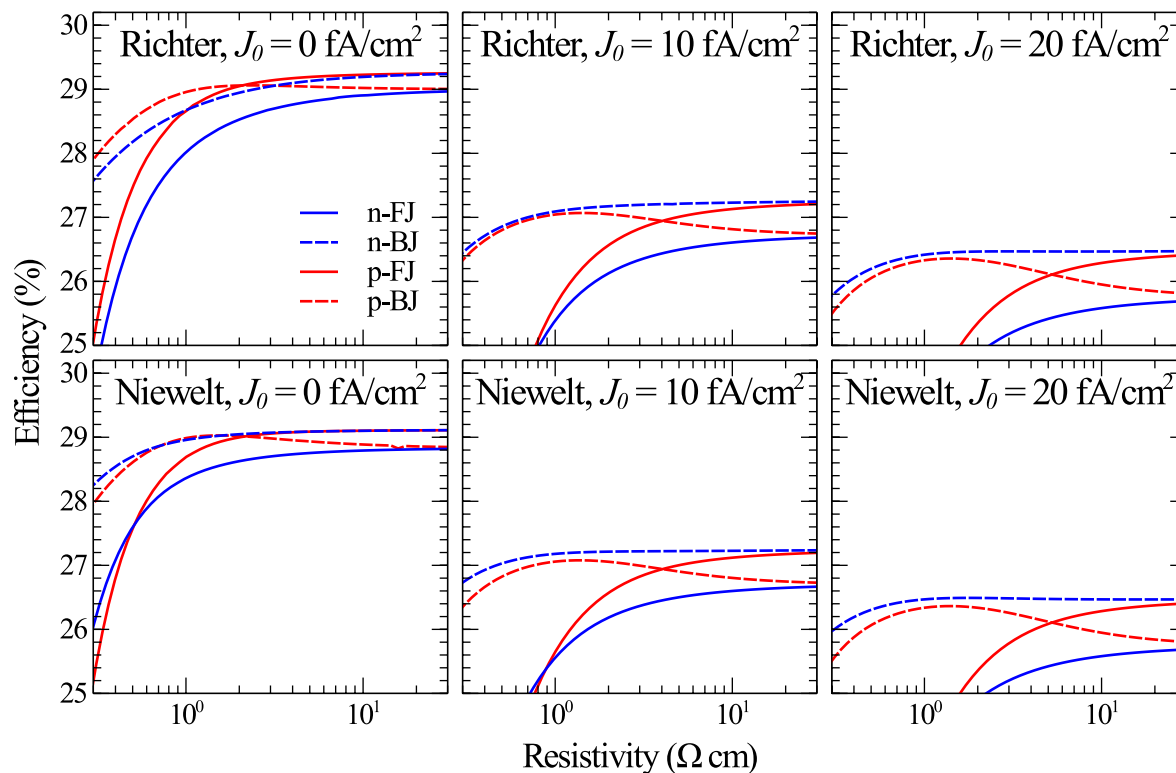


Fig. 6. Simulated (Quokka3) conversion efficiency as a function of wafer resistivity for *n*- and *p*-type front-junction (FJ) and back-junction (BJ) devices with full-area back contact and front line-contacts with a pitch of 1 mm, no front transport layer, and a wafer thickness of 100 μm . Cases are shown using the Auger parameterisations of Richter et al. and of Niewelt et al., and for varying total J_0 .

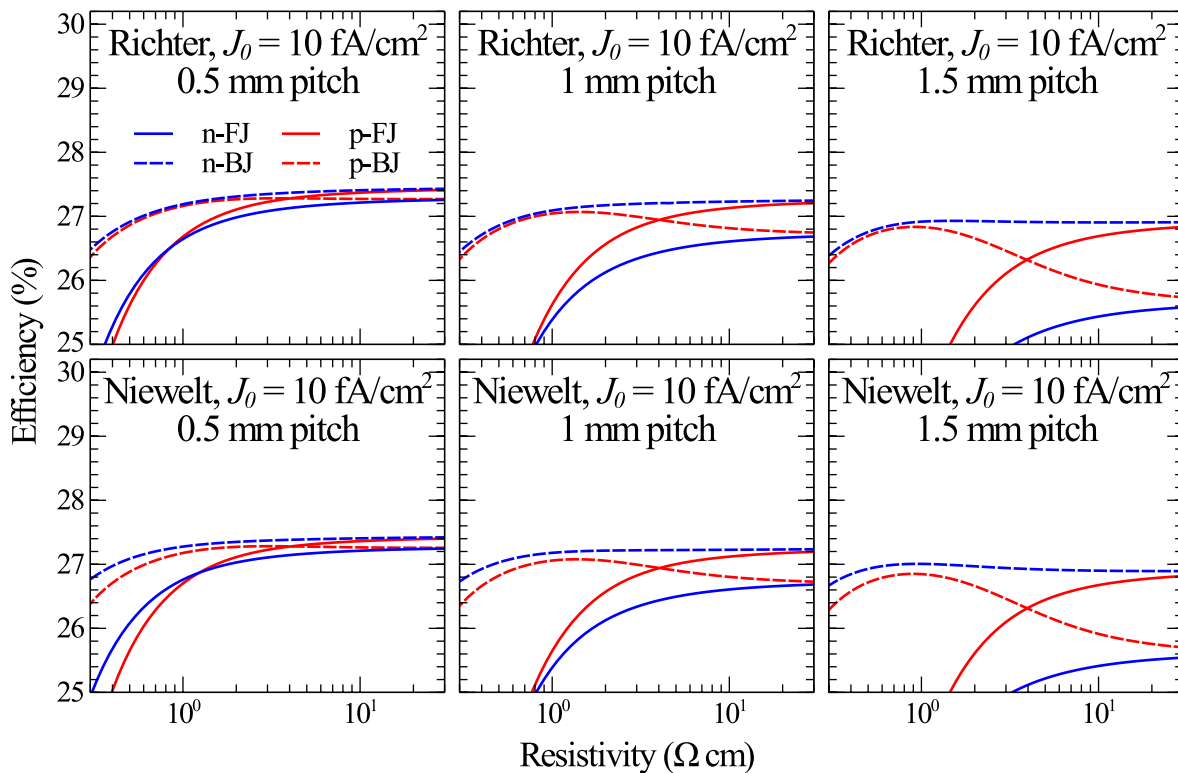


Fig. 7. Simulated (Quokka3) conversion efficiency as a function of wafer resistivity for *n*- and *p*-type front-junction (FJ) and back-junction (BJ) devices with full-area back contact and front line-contacts with variable pitch, no front transport layer, a wafer thickness of 100 μm, and a total $J_0 = 10 \text{ fA/cm}^2$. Cases are shown using the Auger parameterisations of Richter et al. and of Niewelt et al.

this question, in Fig. 8 we plot contour plots of simulated efficiency for *n*- and *p*-type back-junction cells with a 1 mm front-contact pitch and total J_0 of 10 fA/cm², as a function of both resistivity and wafer thickness, using the Auger model of Niewelt et al. We also plot the resulting efficiency difference between the *n*- and *p*-type devices at a given resistivity and thickness.

It can be seen that although both the efficiency and the useable resistivity range improve with increasing thickness for the *p*-type back-junction devices, the efficiency of the *n*-type back-junction devices also improves, and they retain an advantage over the *p*-type over the examined range (albeit reduced at higher thicknesses).

We have seen that the intrinsic advantage of *n*-type back junction devices increases with increasing surface J_0 and contact pitch. In order to more thoroughly quantify the influence of these parameters, and to better define the conditions under which *p*-type back-junction devices may be expected to close the performance gap, in Fig. 9 we plot contour plots of simulated efficiency for *n*- and *p*-type back-junction cells with a resistivity of 1.5 Ω cm and thickness of 160 μm, as a function of both front-contact pitch and J_0 , using the Auger model of Niewelt et al. The thickness is chosen as representative of current industry trends, while the resistivity value is close to the optimum for the *p*-type devices based on Fig. 8. We again also plot the resulting efficiency difference between

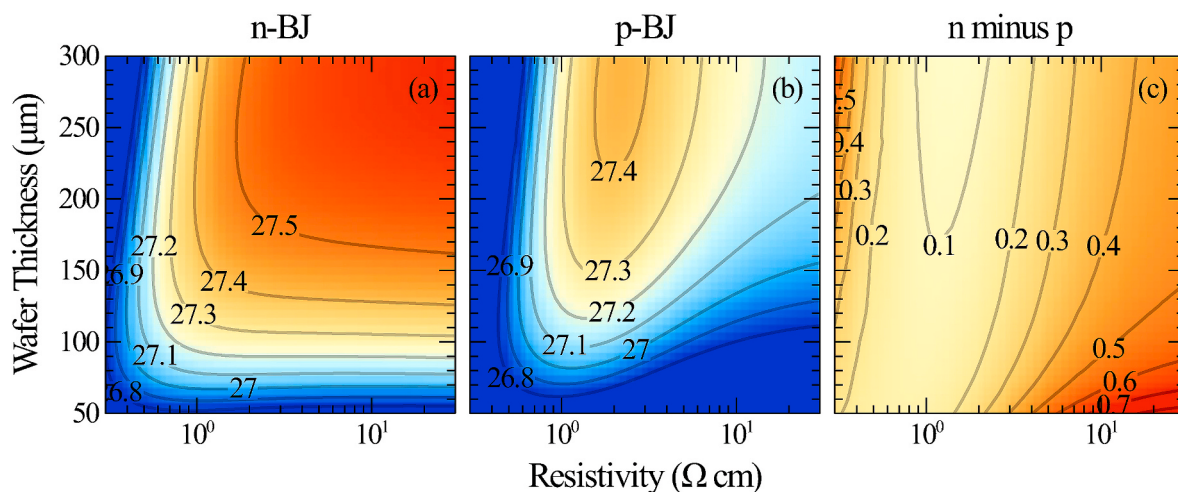


Fig. 8. Simulated (Quokka3) conversion efficiency (%) as a function of wafer resistivity and thickness for a) *n*-type back-junction and b) *p*-type back-junction devices with a front contact pitch of 1 mm and total J_0 of 10 fA/cm², using the Auger model of Niewelt et al. c) Efficiency difference between a) and b) (*n*-type minus *p*-type efficiency).

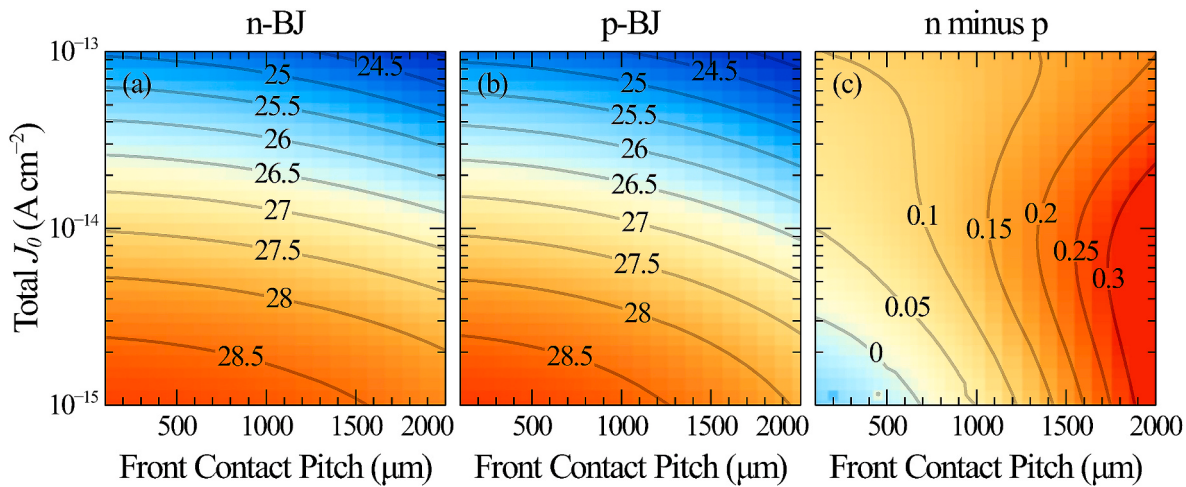


Fig. 9. Simulated (Quokka3) conversion efficiency (%) as a function of front contact pitch and total surface J_0 for a) *n*-type back-junction and b) *p*-type back-junction devices with a resistivity of $1.5 \Omega \text{ cm}$ and wafer thickness of $160 \mu\text{m}$, using the Auger model of Niewelt et al. c) Efficiency difference between a) and b) (*n*-type minus *p*-type efficiency).

the *n*- and *p*-type devices at a given resistivity and thickness.

It can be seen that the *p*-type back-junction device only matches the intrinsic performance potential of the *n*-type device for very low values of J_0 and contact pitch. Such values of J_0 would be exceedingly challenging to achieve in practice on a device level, though perhaps not impossible. More important to remember is that this comparison has been made at a resistivity close to the (relatively narrow) optimum for the *p*-type device, while the *n*-type device offers a much greater tolerance for resistivity variation that is also less sensitive to surface recombination and pitch.

Of course, it should be emphasised that actual performance potential will depend on technologically achievable extrinsic losses, including bulk Shockley–Read–Hall recombination, which is different for the same defects in *n*- and *p*-type Si [13], as well as J_0 of available *n*- and *p*-type passivation/contact layers, which may also not all be interchangeable between the front and rear of devices (e.g. because of parasitic absorption losses). We have also been considering devices with a full-area back contact, whereas industry devices would more likely use line-contacts on both sides both to improve bifaciality and to reduce metal consumption. However, the full-area back contact could in principle be replaced by an external transport layer on the back side, where parasitic absorption is much less of an issue than on the front side.

2.3. Transport layers

Finally, it seems worthwhile to consider the question of whether highly doped *n*- or *p*-type Si offer any intrinsic advantage as transport layers for Si cells, since the Auger parameters in this range have also been revised in the parameterisations of Black & Macdonald and Niewelt et al. (even though the ratio of the Auger coefficients has not significantly changed, as shown in Fig. 1). For this application, it is desirable to minimize both the sheet resistance R_{sheet} of the heavily doped layer, as well J_0 resulting from Auger recombination in this layer. R_{sheet} can be calculated from

$$R_{sheet}^{-1} = q \int_0^{x_j} (n_0, p_0) \mu_{maj} dx \quad (4)$$

where x_j is the junction depth of the heavily doped region, μ_{maj} is the (doping-dependent) majority carrier mobility, and (n_0, p_0) indicates the equilibrium majority carrier concentration (n_0 in *n*-type Si, p_0 in *p*-type). Meanwhile, following the definition of J_0 [14] and assuming low-injection conditions ($\Delta n \ll n_0 + p_0$) far from equilibrium ($pn \gg n_{i,eff}^2$),

J_0 can be calculated simply from

$$J_0 = q \int_0^{x_j} \frac{n_{i,eff}^2}{(n_0, p_0) \tau_{eff}} dx \quad (5)$$

which is valid under the condition that the quasi-Fermi levels are flat through the heavily doped region (this will obtain to a good approximation when J_0 is sufficiently low, as for most layers of practical interest when the surface is passivated). When Auger recombination is dominant, $\tau_{eff}^{-1} \approx C_{n,p} (n_0, p_0)^2$ (where $C_{n,p}$ denotes the Auger coefficient for the majority carrier process), and we can write

$$J_0 = q \int_0^{x_j} n_{i,eff}^2 C_{n,p} (n_0, p_0) dx \quad (6)$$

We note that R_{sheet} is inversely proportional to the thickness of the layer, while J_0 is proportional to thickness. A useful figure of merit is therefore the product of J_0 and R_{sheet} , which has units of V cm^{-2} , and importantly, under the above conditions, is independent of layer thickness. In the case of uniform doping the integrals can be dispensed with and the product can be written simply as

$$J_0 R_{sheet} = \frac{n_{i,eff}^2 C_{n,p}}{\mu_{maj}} \quad (7)$$

Since it is desirable to minimize both J_0 and R_{sheet} , it is also desirable to minimize their product. Within the constraints of this product, decreases in J_0 or R_{sheet} can be obtained at the cost of corresponding increases in the other by varying the thickness or depth of the heavily doped region.

Fig. 10a shows the resulting values of $J_0 \times R_{sheet}$ as a function of equilibrium majority carrier concentration in heavily doped Si at 300 K. For uniform doping, this quantity increases with carrier concentration above 10^{18} cm^{-3} , before peaking at a very similar value of $J_0 \times R_{sheet} \approx 4.5 \times 10^{-12} \text{ V cm}^{-2}$ at carrier concentrations close to $\sim 10^{20} \text{ cm}^{-3}$ for both *n*- and *p*-type Si. This increase is due both to the increase of $n_{i,eff}$ due to bandgap narrowing, as well as the reduction of μ_{maj} with increasing carrier concentration. At higher concentrations $J_0 \times R_{sheet}$ again decreases rapidly because of the decrease in $n_{i,eff}$ due to the onset of carrier degeneracy. Note that full numerical simulations using EDNA2 [15] resulted in excellent agreement with these values, so long as profile thicknesses were kept sufficiently low (for thicker profiles $J_0 \times R_{sheet}$ will be somewhat reduced due to recombination becoming limited by minority-carrier transport). Fig. 10b shows the ratio of $J_0 \times R_{sheet}$ for

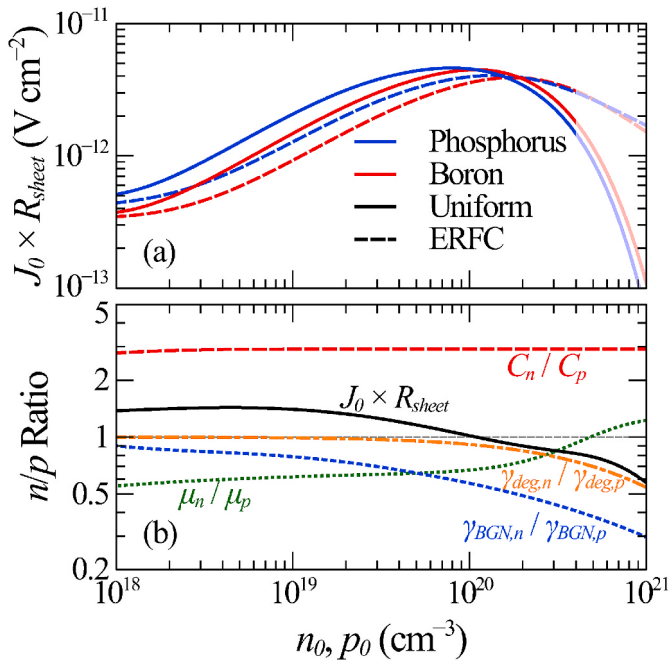


Fig. 10. a) Implied $J_0 \times R_{sheet}$ product as a function of equilibrium majority carrier concentration (n_0 or p_0) for n- and p-type Si in the doping range relevant for heavily doped n + or p + transport layers, both for uniform doping and for complementary error function (ERFC) concentration profiles. Darker lines indicate the approximate active dopant concentration limit resulting from diffusion at 1100°C . b) Ratio between the $J_0 \times R_{sheet}$ product for uniformly doped n- and p-type Si as a function of the equilibrium majority carrier concentration, together with the component ratios which compose it: Auger coefficients (C_n/C_p), majority carrier mobilities (μ_n/μ_p), band-gap narrowing (γ_{BGN}), and degeneracy factors (γ_{deg}) (the latter two defined as in Ref. [16]).

n-type Si to that in p-type Si as a function of carrier concentration for uniform doping, as well as the individual contributions to this ratio due to differences in the Auger coefficients, mobility, bandgap narrowing, and degeneracy. It can be seen that the net effect of the latter components tends to largely compensate the influence of the Auger coefficient ratio.

Since for lateral transport applications it is desirable to minimize $J_0 \times R_{sheet}$, the sharp reduction at high concentrations may at first appear promising. However in practice it is difficult to exploit the expected properties of silicon at this doping level because of practical limitations regarding achievable i) dopant levels, and ii) dopant profiles. Active dopant concentrations achievable using diffusion processes at or below 1100°C are limited to $\sim 4 \times 10^{20} \text{ cm}^{-3}$ for both boron and phosphorus dopants [17,18] (in the case of phosphorus this is due to the solid solubility limit, while for boron supersaturation is observed). Furthermore, perfectly abrupt dopant profiles cannot be realized experimentally. Non-abrupt profiles include portions with lower carrier concentrations, for which the specific $J_0 \times R_{sheet}$ product may be higher or lower. Integration over such profiles will therefore result in a smoothing out of differences in $J_0 \times R_{sheet}$ between the extremes.

To illustrate this, in Fig. 10a we also show $J_0 \times R_{sheet}$ calculated for complementary error function (ERFC) carrier profiles with surface concentrations equal to the specified carrier concentration. ERFC dopant profiles are expected to result from a constant-source diffusion with a constant dopant diffusion coefficient, and are observed experimentally e.g. for lighter phosphorus diffusions. It is important to reiterate here that because of the properties of the $J_0 \times R_{sheet}$ product, this quantity is independent of the assumed profile depth (regardless of the profile shape), and so these results are quite general with respect to profile depth. It can be seen that this indeed results in a smoothing out of the sharp decrease in $J_0 \times R_{sheet}$ observed at high dopant concentrations for

uniform doping. When one also takes into account the practical upper limit to the achievable surface dopant concentrations, the minimum value of $J_0 \times R_{sheet}$ at the high concentration end is limited to $\sim 3 \times 10^{-12} \text{ V cm}^{-2}$ in both n- and p-type Si. Consequently, the lower dopant concentration range is the area to focus on when seeking to minimize $J_0 \times R_{sheet}$.

Note that in these calculations we have assumed an ERFC profile for the equilibrium majority carrier concentration (n_0 or p_0). Due to incomplete ionisation effects [19], n_0 and p_0 are expected to be somewhat smaller than the active dopant concentration N , especially for N close to $2 \times 10^{18} \text{ cm}^{-3}$, and an ERFC dopant profile will therefore give rise to a carrier concentration profile that deviates somewhat from a strict ERFC profile. However, because of the averaging effect resulting from the integration in (4)–(6), this has only a fairly minor effect on the resulting $J_0 \times R_{sheet}$ product. Indeed, the use of a different profile shape, such as a Gaussian distribution, or even a “ $1 - Y^{2/3}$ ” profile as observed experimentally for boron diffusions in silicon [20], was found to result in only minor changes to $J_0 \times R_{sheet}$ compared to an ERFC profile.

Rather than comparing n- and p-type profiles with the same surface concentration, it arguably makes more sense to compare profiles of the same effective resistivity, i.e. the same sheet resistance for a given profile depth, since practically achievable profile depth is an important factor limiting achievable $J_0 \times R_{sheet}$ values in commercial devices. Note that we use resistivity and not sheet resistance here because the former, like the $J_0 \times R_{sheet}$ product, is independent of profile depth, which allows the results to remain generally applicable. In Fig. 11a and Fig. 11b we plot $J_0 \times R_{sheet}$ vs effective resistivity for n- and p-type Si with both uniform and ERFC profiles. Fig. 11c again shows the various contributions to the ratio between $J_0 \times R_{sheet}$ for n-to that for p-type, but in this case as a function of resistivity. What is striking is the extremely similar dependence of $J_0 \times R_{sheet}$ on effective resistivity for n- and p-type Si, regardless of the profile. In particular, the minimum achievable values for $J_0 \times R_{sheet}$ at the low-doping/high-resistivity end are very similar, at around $3\text{--}4 \times 10^{-13} \text{ V cm}^{-2}$. This suggests that there is little intrinsic advantage expected for either highly doped n-type or highly doped p-type Si as a transport layer material based on current models for the relevant material properties. However, it should be noted that the corresponding doping range ($<\sim 10^{18} \text{ cm}^{-3}$) features the greatest uncertainty in C_n and C_p for current Auger models [2], with both changing rapidly with doping in this range due to the onset of screening effects.

3. Conclusion

In light of recent revisions to the Auger parameterisation in Si, we have considered the question of whether this is expected to result in an intrinsic advantage for either n- or p-type Si solar cells, either generally, or for specific architectures. We find that the revised models predict a relative improvement in the intrinsic performance potential of n-type devices compared to the previous parameterisation of Richter et al. p-type devices retain an intrinsic advantage only when i) surface recombination can be kept extremely low, and majority carrier transport losses are small, or ii) when minority carrier transport losses limit performance. The latter case may obtain in front-junction devices, where lightly-doped p-type devices can tolerate a less conductive front transport layer thanks to the higher conductance contribution of their bulk minority carriers. The advantage of n-type devices tends to increase both with increasing surface recombination and with increased demands on majority-carrier transport. In particular, n-type both-sides-contacted back-junction devices without a front transport layer show both higher efficiency potential and significantly reduced sensitivity to resistivity variation than equivalent p-type devices, due especially to reduced lateral majority-carrier transport losses. Finally, we find no clear intrinsic performance advantage for either highly doped n-type or p-type Si as transport layers for Si cells.

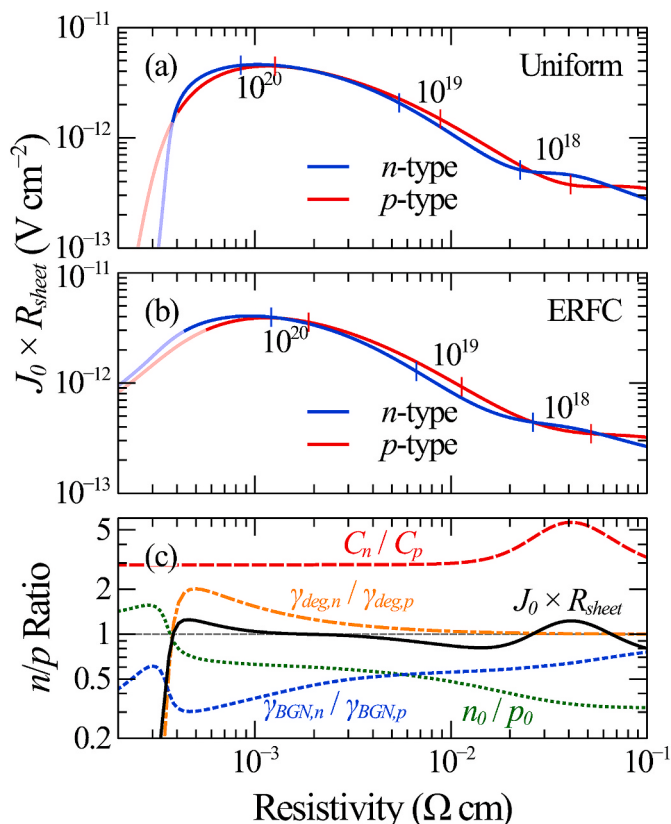


Fig. 11. Implied $J_0 \times R_{sheet}$ product as a function of resistivity for n - and p -type Si in the doping range relevant for heavily doped n + or p + transport layers, for a) uniform doping and b) complementary error function (ERFC) concentration profiles. In the case of the ERFC profiles, the given resistivity is equal to the sheet resistance multiplied by the depth factor. Corresponding carrier concentrations are marked at intervals, and labelled in units of cm^{-3} . Darker lines indicate the approximate active dopant concentration limit resulting from diffusion at 1100°C . c) Ratio between the $J_0 \times R_{sheet}$ product for uniformly doped n - and p -type Si as a function of resistivity, together with the component ratios which compose it: Auger coefficients (C_n/C_p), carrier concentrations (n_0/p_0), band-gap narrowing (γ_{BGN}), and degeneracy factors (γ_{deg}) (the latter two defined as in Ref. [16]).

CRediT authorship contribution statement

Lachlan E. Black: Writing – original draft, Visualization, Investigation, Conceptualization. **Daniel H. Macdonald:** Writing – review & editing, Supervision, Funding acquisition.

Declaration of competing interest

The authors declare that they have no known competing financial interests or personal relationships that could have appeared to influence the work reported in this paper.

Data availability

Data will be made available on request.

Acknowledgements

This work was supported by the Australian Renewable Energy Agency (ARENA) through project 2017/RND017.

References

- [1] A. Richter, S.W. Glunz, F. Werner, J. Schmidt, A. Cuevas, Improved quantitative description of Auger recombination in crystalline silicon, *Phys. Rev. B* 86 (Oct 2012).
- [2] L.E. Black, D.H. Macdonald, On the quantification of Auger recombination in crystalline silicon, *Sol. Energy Mater. Sol. Cell.* 234 (2022), 111424.
- [3] T. Niewelt, B. Steinhäuser, A. Richter, B. Veith-Wolf, A. Fell, N.E. Grant, L.E. Black, J.D. Murphy, M.C. Schubert, S.W. Glunz, Reassessment of the intrinsic bulk recombination in crystalline silicon, *Sol. Energy Mater. Sol. Cell.* 235C (2022), 111467.
- [4] D.B.M. Klaassen, J.W. Slotboom, H.C. de Graaff, Unified apparent bandgap narrowing in n - and p -type silicon, *Solid State Electron.* 35 (2) (1992) 125–129.
- [5] A. Fell, T. Niewelt, B. Steinhäuser, F.D. Heinz, M.C. Schubert, S.W. Glunz, Radiative recombination in silicon photovoltaics: modeling the influence of charge carrier densities and photon recycling, *Sol. Energy Mater. Sol. Cell.* 230 (2021), 111198.
- [6] R.A. Sinton, A. Cuevas, Contactless determination of current–voltage characteristics and minority-carrier lifetimes in semiconductors from quasi-steady-state photoconductance data, *Appl. Phys. Lett.* 69 (17) (1996) 2510–2512.
- [7] M.J. Kerr, A. Cuevas, R.A. Sinton, Generalized analysis of quasi-steady-state and transient decay open circuit voltage measurements, *J. Appl. Phys.* 91 (1) (2002) 399–404.
- [8] K. Misiakos, D. Tsamakis, Accurate measurements of the silicon intrinsic carrier density from 78 to 340 K , *J. Appl. Phys.* 74 (5) (1993) 3293–3297.
- [9] A. Schenck, Finite-temperature full random-phase approximation model of band gap narrowing for silicon device simulation, *J. Appl. Phys.* 84 (7) (1998) 3684–3695.
- [10] A. Fell, J. Schön, M.C. Schubert, S.W. Glunz, The concept of skins for silicon solar cell modeling, *Sol. Energy Mater. Sol. Cell.* 173 (2017) 128–133.
- [11] H.T. Nguyen, S.C. Baker-Finch, D. Macdonald, Temperature dependence of the radiative recombination coefficient in crystalline silicon from spectral photoluminescence, *Appl. Phys. Lett.* 104 (11) (2014), 112105.
- [12] A. Richter, R. Müller, J. Benick, F. Feldmann, B. Steinhäuser, C. Reichel, A. Fell, M. Bivour, M. Hermle, S.W. Glunz, Design rules for high-efficiency both-sides-contacted silicon solar cells with balanced charge carrier transport and recombination losses, *Nat. Energy* 6 (4) (2021) 429–438.
- [13] J.E. Cotter, J.H. Guo, P.J. Cousins, M.D. Abbott, F.W. Chen, K.C. Fisher, P-type versus n-type silicon wafers: prospects for high-efficiency commercial silicon solar cells, *IEEE Trans. Electron. Dev.* 53 (8) (2006) 1893–1901.
- [14] K.R. McIntosh, L.E. Black, On effective surface recombination parameters, *J. Appl. Phys.* 116 (1) (2014).
- [15] K. McIntosh, P. Altermatt, A freeware 1D emitter model for silicon solar cells, in: Proc. 35th IEEE Photovoltaic Specialists Conf., June 2010, 002188–002193.
- [16] L.E. Black, Degeneracy and bandgap narrowing in the semiconductor electron-hole product, *J. Appl. Phys.* 121 (10) (2017), 105701.
- [17] A. Armigliato, D. Nobili, P. Ostoja, M. Servidori, S. Solmi, Solubility and precipitation of boron in silicon and supersaturation resulting by thermal predeposition, in: *Semiconductor silicon 1977, 77–2*, The Electrochemical Society, 1977, pp. 638–647.
- [18] G. Masetti, D. Nobili, S. Solmi, Profiles of phosphorus predeposited in silicon and carrier concentration in equilibrium with SiP precipitates, in: *Semiconductor silicon 1977, 77–2*, The Electrochemical Society, 1977, pp. 648–657.
- [19] P.P. Altermatt, A. Schenk, G. Heiser, A simulation model for the density of states and for incomplete ionization in crystalline silicon. I. Establishing the model in Si: P, *J. Appl. Phys.* 100 (11) (2006), 113714.
- [20] R.B. Fair, Boron diffusion in silicon-concentration and orientation dependence, background effects, and profile estimation, *J. Electrochem. Soc.* 122 (6) (1975) 800–805.